doi:10.14311/ppt.2025.1.80
Plasma Physics and Technology **12**(1):80–89, 2025

A REVIEW OF NUMERICAL APPROACHES ON DECAYING ARC PLASMAS IN POLYATOMIC C-F-O MOLECULAR GAS FLOW WITH CHEMICAL NON-EQUILIBRIUM CONSIDERATIONS

Yasunori Tanaka

Faculty of Electrical, Information and Communication Eng., Kanazawa University, Kanazawa 920-1192, Japan
tanaka@ec.t.kanazawa-u.ac.jp

Abstract.
This study reviews two numerical models to simulate arc plasma decay in polyatomic molecular gas flows, focusing on chemically non-equilibrium (CNE) effects. The first model addresses C-F-O gas mixtures formed by CO_2 with ablated PTFE vapor, incorporating 24 species and 98 reversible reactions with temperature-dependent rates. It predicts plasma composition and electron density during decay. The second model assumes irreversible $C_5F_{10}O$ decomposition in CO_2/O_2 mixtures, validated by equilibrium analysis. Arc decay under free recovery is analyzed, highlighting the impact of reaction kinetics and gas composition on temperature and species evolution.

Keywords: polyatomic molecular gas, decaying arcs, alternatives for SF_6.

1. Introduction

Gas circuit breakers (GCBs) have long relied on sulfur hexafluoride (SF_6) for its superior dielectric strength and arc-quenching capability. However, due to its extremely high global warming potential (GWP > 23,000), international regulations are accelerating the transition toward eco-friendly alternative gases. Among these, CO_2-based gas mixtures blended with fluorinated additives such as CO_2/C_4F_7N and $CO_2/O_2/C_4F_7N$ as well as $CO_2/O_2/C_5F_{10}O$ are attracting significant interest for use in high-voltage equipment [1–3].

Historically, numerical modeling of arc plasmas has been based on the assumption of local thermodynamic equilibrium (LTE), wherein all species are considered to be in chemical and thermal equilibrium. LTE models have been widely adopted due to their relative simplicity and computational efficiency. They are particularly effective in representing high-current arcs, where rapid collisional processes enforce equilibrium states over short timescales. However, during arc current interruption, particularly in the arc decay phase, plasma conditions can deviate from equilibrium. The arc experiences rapid cooling driven by convection and radiation, while molecular recombination and association reactions often proceed at finite rates. Under these conditions, LTE-based models can lead to significant overestimations of decays in electron density and conductivity, failing to capture the delayed chemical relaxation inherent in polyatomic gas systems.

To address these deficiencies, chemically non-equilibrium (CNE) models have been developed. These models solve additional continuity equations for key species and include reaction kinetics with temperature-dependent rate coefficients. For SF_6 arcs, early CNE modeling efforts incorporated stepwise dissociation of SF_6, SF_4, and other fluorinated species [4]–[5]. The authors also developed two-dimensional (2D) models to simulate decaying SF_6 arc plasmas [6]–[7], N_2 arcs [8], air arcs [9]. including full chemically non-equilibrium models and furthermore two-temperature (2T) chemically non-equilibrium models, both of which predicted both thermal and chemical non-equilibrium states. More recently, studies have extended this framework to alternative gases, such as CO_2 and CO_2/O_2, capturing dissociation chains and recombination in the decaying plasma arcs [10, 11].

One promising research direction is the modeling of decaying arcs in CO_2 mixed with PTFE ablation vapor. Such mixtures involve a complex set of carbon-fluorine-oxygen (C-F-O) species, many of which undergo slow recombination or form stable byproducts like CO, CF, or CF_2. The present authors have developed a CNE model that incorporates 24 species and 98 reversible reactions to simulate such systems with high temporal and spatial resolution [12]. The model successfully captures the decay of electron density and molecular recombination during post-arc cooling. In parallel, to address the computational cost of full CNE models, a simplified approach was proposed for $CO_2/O_2/C_5F_{10}O$ mixtures. Based on equilibrium composition analysis, the dissociation of $C_5F_{10}O$ was modeled as an irreversible reaction, reflecting the fact that recombination is thermodynamically suppressed at lower temperatures [13, 14]. This reduced-order model retains essential features of the thermal and chemical response while being more tractable for engineering simulations.

This paper presents a comparative investigation of these two modeling frameworks. By analyzing the arc decay characteristics under free recovery conditions, we highlight the roles of irreversible decomposition, reaction kinetics, and mixture design in influencing

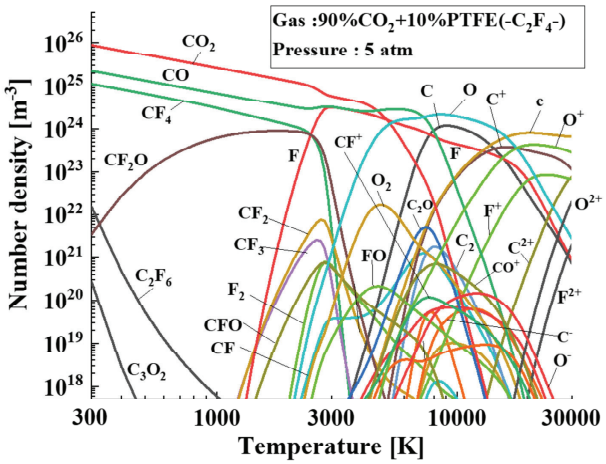

Figure 1. Equilibrium composition of 90%CO_2 + 10%C_2F_4 vapor considering 48 species [12].

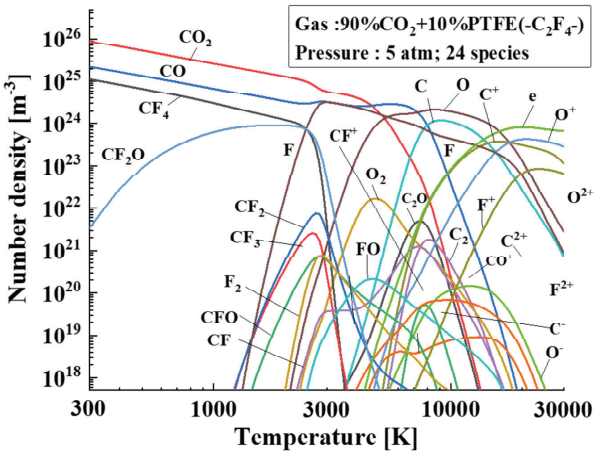

Figure 2. Equilibrium composition of 90%CO_2 + 10%C_2F_4 vapor considering 24 species [12].

arc quenching behavior.

2. Modeling of Arc Plasmas in the C-F-O System with Chemically Non-Equilibrium Effects

2.1. Selection of Dominant Species

To construct a chemically non-equilibrium (CNE) model for decaying arc plasmas in CO_2 mixed with PTFE vapor (C_2F_4), it is essential to identify dominant species that significantly influence arc chemistry over a wide temperature range. As a preliminary step, equilibrium composition calculations were performed using the NIST-JANAF thermochemical tables [15], assuming a 90%CO_2 + 10%C_2F_4 vapor mixture at 0.5 MPa. The analysis considered 48 species composed of carbon (C), fluorine (F), and oxygen (O) atoms.

Figure 1 shows the calculated equilibrium composition, highlighting CO_2, CO, and CF_4 as major species below 4000 K. At higher temperatures, dissociation produces radicals and atoms such as C, F, and O. Beyond 8000 K, ionization becomes prominent, generating C^+, F^+, O^+, and free electrons.

From this full set, 24 chemically significant species were selected for the CNE model: CF_4, CF_3, CF_2, CF, CF_2O, CO_2, CO, C_2O, C_2, C_3, F_2, O_2, C, F, O, O_2^+, C^+, F^+, F^-, O^+, O^-, and e^-. These species are sufficient to capture the major kinetic pathways under arc and post-arc conditions. Figure 2 confirms that the simplified 24-species model reproduces the qualitative composition trends of the full 48-species system, justifying the species reduction.

2.2. Governing Equations

Because of fundamental study, for simplicity, the behavior of arc plasmas is modeled under the assumptions of axial symmetry, laminar flow due to slower gas flow velocity compared to circuit breakers, optically thin radiation, and no surface evaporation or electron emission from electrodes. The following conservation equations describe the coupled evolution of mass, momentum, energy, and species mass fractions:
Mass:

$$\frac{D\rho}{Dt} = -\rho(\nabla \cdot \boldsymbol{u}), \tag{1}$$

Momentum:

$$\rho\frac{D\boldsymbol{u}}{Dt} = -\nabla p + \nabla \cdot \bar{\tau}, \tag{2}$$

$$\bar{\tau} = \tau_{ij} = 2\eta\{e_{ij} - \frac{1}{3}\delta_{ij}(\nabla \cdot \boldsymbol{u})\} \tag{3}$$

Energy:

$$\rho C_{\mathrm{v}}\frac{DT}{Dt} = -p(\nabla \cdot \boldsymbol{u}) + \nabla \cdot (\lambda_{\mathrm{tr}}\nabla T) + Q_{\mathrm{heat}} \tag{4}$$

$$Q_{\mathrm{heat}} = \sum_{j=1}^{N}\nabla \cdot (\rho D_j h_j \nabla Y_j) + \sum_{\ell}^{L}\Delta Q_\ell - P_{\mathrm{rad}} \tag{5}$$

Mass of species j:

$$\rho\frac{DY_j}{Dt} = \nabla \cdot (\rho D_j \nabla Y_j) + S_j, \tag{6}$$

$$S_j = m_j \sum_{\ell}^{L}(\beta^{\mathrm{r}}_{j\ell} - \beta^{\mathrm{f}}_{j\ell})(k^{\mathrm{f}}_\ell \prod_{i=1}^{N} n_i^{\beta^{\mathrm{f}}_{i\ell}} - k^{\mathrm{r}}_\ell \prod_{i=1}^{N} n_i^{\beta^{\mathrm{r}}_{i\ell}}) \tag{7}$$

The equation of state:

$$\rho = \frac{p}{\kappa T \sum_j^N \frac{Y_j}{m_j}} \tag{8}$$

where ρ: mass density, t: time, $\boldsymbol{u}$: gas flow vector, p: pressure, $\bar{\tau}$: stress tensor, η: viscosity, e_{ij}: the rate of deformation tensor, δ_{ij}: Kronecker delta, T: temperature, C_{v}: effective specific heat at constant volume, λ_{tr}: translational thermal conductivity, D_j: effective diffusion coefficient, h_j: enthalpy of species j, Y_j: mass fraction of species j, P_{rad}: radiation power, ΔQ_ℓ: heating power from reaction heat of reaction ℓ,

$CO_2 + O \rightarrow CO + O_2$	$CO_2 + C \rightarrow CO + CO$
$CO_2 + M \rightarrow CO + O + M$	$CO + C + M \rightarrow C_2O + M$
$CO + M \rightarrow C + O + M$	$C + C + M \rightarrow C_2 + M$
$C_2 + C_2 \rightarrow C_3 + C$	$C_2O + O \rightarrow CO + CO$
$C_2O + O_2 \rightarrow CO_2 + CO$	$CO_2 + e \rightarrow CO + O + e$
$C + e \rightarrow C^+ + e + e$	$O_2 + M \rightarrow O + O + M$
$O_2 + e \rightarrow O^- + O$	$O_2 + e \rightarrow O + O + e$
$O_2 + e \rightarrow O_2^+ + e + e$	$O^- + C \rightarrow O + e + e$
$O_2^+ + e \rightarrow O + O$	$O^- + O_2^+ \rightarrow O + O_2$
$O^- + O_2^+ \rightarrow O + O + O$	$O_2 + e \rightarrow O^- + O^+ + e$
$O_2 + e \rightarrow O + O^+ + 2e$	$O + e \rightarrow O^+ + e + e$
$O^- + O^+ \rightarrow O + O$	$O^+ + O_2 \rightarrow O + O_2^+$
$CF + O \rightarrow CO + F$	$CF + F \rightarrow C + F_2$
$CF + F + M \rightarrow CF_2 + M$	$CF_3 + F + M \rightarrow CF_4 + M$
$F + F + M \rightarrow F_2 + M$	$CF_2 + F + M \rightarrow CF_3 + M$
$FCO + F \rightarrow CO + F_2$	$FCO + F \rightarrow COF_2$
$COF_2 + F \rightarrow FCO + F_2$	$CF_2 + O \rightarrow FCO + F$
$CF_2 + O_2 \rightarrow COF_2 + O$	$CF_2 + F_2 \rightarrow CF_3 + F$
$CF_2 \rightarrow CF + F$	$OF + O \rightarrow O_2 + F$
$OF + OF \rightarrow O_2 + F + F$	$OF + OF \rightarrow F_2 + O_2$
$CO + OF \rightarrow CO_2 + F$	$COF_2 + CO \rightarrow FCO + FCO$
$F + e \rightarrow F^+ + 2e$	$F + F + F \rightarrow F_2 + F$
$2F_2 \rightarrow 2F + F_2$	$F_2 + e \rightarrow F + F + e$
$F^- + F \rightarrow F + F + e$	$F^+ + F^- + F \rightarrow F_2 + F$
$F^- + F \rightarrow F_2 + e$	

Table 1. Reactions considered in the chemically non-equilibrium model of C-F-O system arc plasmas [12].

m_j: mass of species j, $\beta_{j\ell}$: stoichiometric coefficient of species j for reaction ℓ, $k_\ell^{\mathrm{f,r}}$: reaction rate coefficient for reaction ℓ, n_j: density of species j, κ: Boltzmann constant, $\frac{D}{Dt} = \frac{\partial}{\partial t} + \boldsymbol{u}\cdot\nabla$ is the Lagrangian derivative. Solving (6) enables calculation of particle composition in the CO_2+C_2F_4 arc plasma under chemically non-equilibrium condition considering reaction rates.

2.3. Reaction Set and Transport Properties

A total of 98 reactions (49 forward and 49 reverse) are included in the model, covering key electron-impact ionization, dissociation, association, and electron attachment/detachment reactions (see Table 1). Forward rate coefficients are taken from NIST and other literature sources, while reverse rates are derived by the principle of detailed balance. Transport coefficients, including thermal conductivity λ_{tr}, viscosity η, and binary diffusion coefficients D_j, are evaluated using the Chapman-Enskog method with first-order approximation. Radiative losses P_{rad} account for lines including atomic lines and ion lines and continuum contributions from bremsstrahlung and the recombination radiation.

2.4. Computational Domain and Conditions

Figure 3 illustrates the axisymmetric r-z computational domain. The nozzle and electrodes are modeled with thermal boundary conditions, but material evaporation is neglected. Boundary conditions are defined as follows: At Inlet ($z = 0\,\mathrm{mm}$), $T = 300\,\mathrm{K}$, $u_z = 5\,\mathrm{m/s}$, species concentrations from equilibrium; At Outlet, zero-gradient boundary conditions, $p = 0.5\,\mathrm{MPa}$; On the Axis ($r = 0$), symmetry condition was set; At Wall (nozzle and electrodes), no-slip ($u = 0$), thermal conduction allowed.

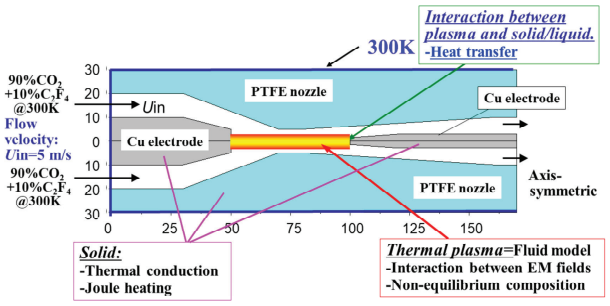

Figure 3. Calculation domain.

Simulations are carried out in two stages. First, a steady-state arc is calculated for 100 A using the SIMPLE algorithm. Next, a transient simulation is performed under free recovery conditions with current instantaneously dropping from 100 A to 0 A at $t = 0\,\mu\mathrm{s}$ using the CIP-CUP method.

2.5. Results of CO_2 gas [11]

2.5.1. Temperature variation

Figure 4 illustrates the temporal evolution of arc temperature in a CO_2 gas flow. The temperature distribution is visualized using color contours ranging from 300 K to 5000 K on a logarithmic scale. The inlet gas velocity was set to 5 m/s, corresponding to a volumetric flow rate of approximately 280 L/min.

Figure 4(a) shows the steady-state temperature field at a current of 100 A ($t = 0\,\mu\mathrm{s}$). The arc core reaches a peak temperature of approximately 18,000 K along the axis, with the high-temperature region extending radially up to 2.5 mm. Hot gas at around 3000 K is convected downstream, resulting in elevated gas temperatures near the downstream electrode. The electrode surface temperature reaches approximately 2000 K on the upstream (left-hand) side and 3000 K on the downstream (right-hand) side, indicating asymmetric thermal loading.

Under free recovery conditions following current interruption at $t = 0\,\mu\mathrm{s}$, the arc enters a transient cooling phase. The temperature near the nozzle throat inlet ($z = 70\,\mathrm{mm}$) drops rapidly due to high local gas velocities that enhance convective heat loss. As a result, the arc plasma begins to constrict around the nozzle throat, a behavior particularly evident for $t > 50\,\mu\mathrm{s}$. By $t = 100\,\mu\mathrm{s}$, cold gas from the surroundings begins to penetrate into the arc region, and by $t = 200\,\mu\mathrm{s}$, the arc column has significantly thinned, indicating ongoing plasma recombination and cooling in the decaying arc.

2.5.2. Time Variation in CO_2 Mole Fraction

Figure 5 shows the temporal evolution of the CO_2 mole fraction distribution under free recovery conditions. The mole fraction is visualized using a color scale ranging from 10^{-8} to 10^{0}.

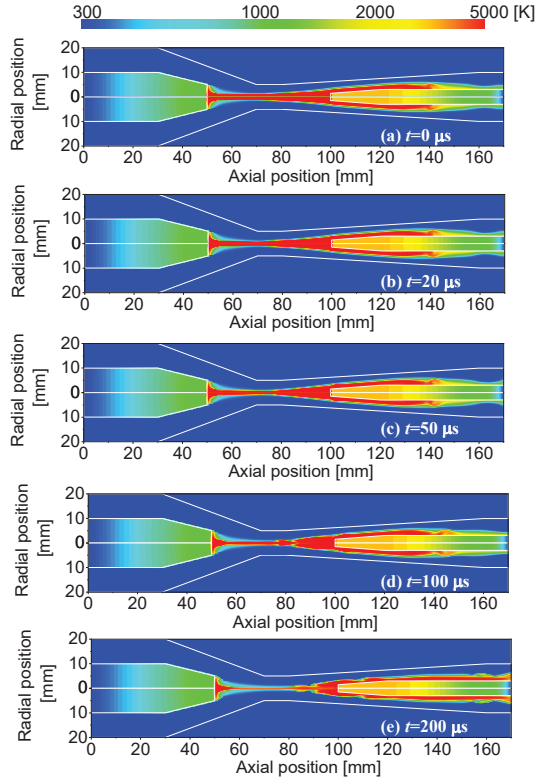

Figure 4. Temperature variation in 100%CO_2 arc under free recovery condition (100→ 0 A, CO_2 gas velocity 5 m/s) [11].

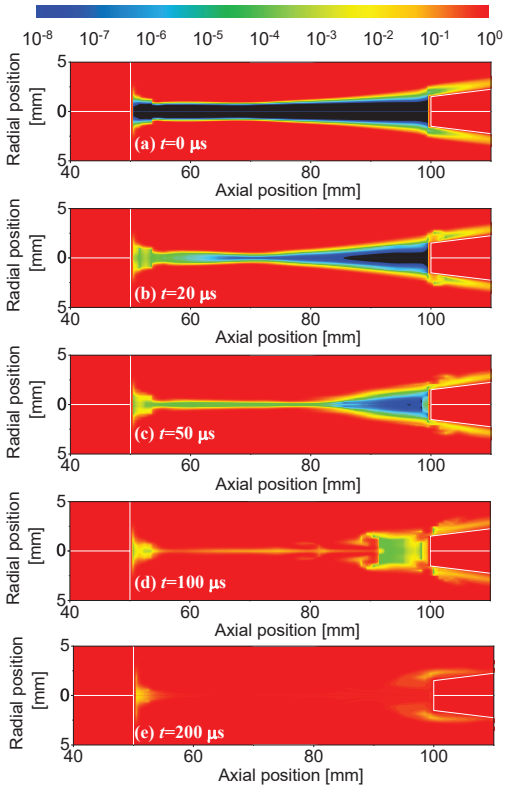

Figure 5. Time variation in distribution of mole fraction of CO_2 under free recovery condition (100→ 0 A, CO_2 gas velocity 5 m/s) [11].

Figure 5(a) displays the steady-state distribution at a current of 100 A ($t = 0\,\mu s$). In the high-temperature region near the arc axis, the CO_2 molecules are almost completely dissociated, resulting in a negligible mole fraction at the arc core. A sharp increase in CO_2 mole fraction is observed in the radial range of $r = 1$–2 mm, and beyond $r \geq 2$ mm, the mole fraction approaches unity. This indicates a steep compositional gradient at the arc boundary, where undissociated ambient CO_2 transitions to a fully dissociated plasma core.

Figures 5(b)–(e) present the transient evolution of CO_2 mole fraction following current interruption. As the arc cools, CO_2 molecules rapidly re-form due to recombination processes. By $t = 20\,\mu s$, the CO_2 mole fraction reaches values above 10^{-4} at the nozzle throat inlet ($z \approx 70$ mm), where the gas velocity is highest and convective cooling is most intense. At $t = 50\,\mu s$, the CO_2 mole fraction further increases to approximately 0.1 near the nozzle throat exit.

As the arc continues to decay, molecular recombination progresses. By $t = 100\,\mu s$, CO_2 recovery is evident even along the arc axis. At $t = 200\,\mu s$, CO_2 is nearly fully restored throughout the computational domain, indicating that the gas has reverted to its initial molecular composition after complete plasma extinction.

2.5.3. Time Variation in CO Mole Fraction

Figure 6 illustrates the temporal evolution of the CO mole fraction during arc decay in a CO_2 gas-blast under free recovery conditions. As the arc temperature decreases, particularly along the arc periphery, the mole fraction of CO increases due to the partial recombination of dissociated CO_2.

At $t = 20\,\mu s$, this trend is especially prominent near the nozzle throat inlet around $z = 70$ mm, where elevated gas velocity enhances convective heat loss, resulting in a rapid local temperature drop. In this region, the CO mole fraction exceeds 10^{-4}, primarily concentrated along the outer regions of the arc.

By $t = 50\,\mu s$, the CO mole fraction further increases to approximately 0.01–0.1 at the nozzle throat exit. As the arc continues to decay, CO formation progresses inward. At $t = 100\,\mu s$, significant CO presence is observed even along the arc axis, indicating that recombination reactions are occurring throughout the plasma volume.

At $t = 200\,\mu s$, however, the CO mole fraction decreases across most of the domain. This decline is attributed to secondary chemical reactions in which CO combines with atomic oxygen (O) to re-form CO_2, signaling the gradual restoration of the initial molecular composition as thermal equilibrium is approached.

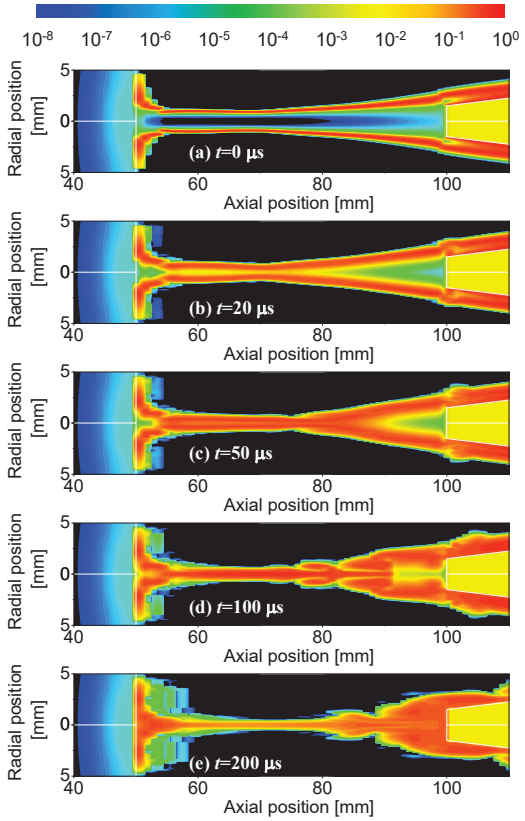

Figure 6. Time variation in distribution of mole fraction of CO under free recovery condition (100→ 0 A, CO_2 gas velocity 5 m/s) [11].

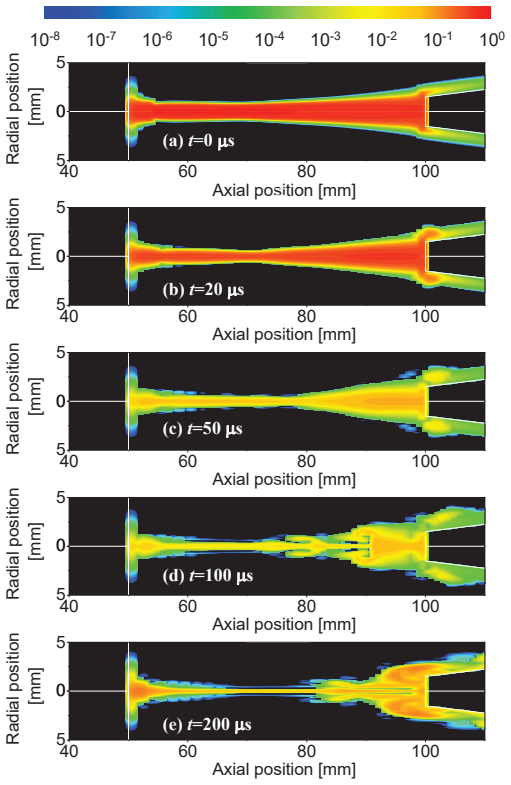

Figure 7. Time variation in distribution of electron mole fraction under free recovery condition (100→ 0 A, CO_2 gas velocity 5 m/s) [11].

2.5.4. Time Variation in Electron Mole Fraction

Figure 7 presents the spatial distribution of the electron mole fraction in the CO_2 gas-blast arc under free recovery conditions. The color scale is defined over the range of 10^{-8} to 10^{0}.

At the initial time ($t = 0\,\mu s$), corresponding to steady-state conditions with a current of 100 A, the electron mole fraction is high in the arc core. This is due to the ionization of carbon and oxygen atoms in the high-temperature region along the arc axis, resulting in a dense electron population.

As the arc begins to decay over the time interval $t = 0$–$100\,\mu s$, the gas temperature decreases due to convection and radiation losses. Consequently, the electron mole fraction drops rapidly with time. By $t = 100\,\mu s$, the electron mole fraction has decreased to approximately 10^{-4} along the arc axis.

At $t = 200\,\mu s$, the cooling process continues, and the electron mole fraction further declines to around 10^{-6} at the arc center. This reduction reflects both the recombination of charged species and the loss of thermal ionization capability as the plasma transitions into a predominantly neutral gas.

2.5.5. Comparison of changes in particle mole fraction between NCE model and LTE model

Figure 8 compares time variations in mole fraction of CO_2, CO, O_2, O, and electrons at $t = 100\,\mu s$ in the free recovery condition. This is a comparison of the calculation results of the NCE model with the LTE model. From the figure, the mole fractions of CO and O show almost the same distributions and values between the NCE and LTE models. On the other hand, CO_2, O_2, and e give large differences. In particular, the recovery of CO_2 was delayed in the vicinity of the downstream electrode in the NCE model. This is because the association reaction for producing CO_2 molecules is delayed with time because the association reaction occurs at low temperatures. As for O_2, the NCE model indicates that more O_2 is generated than the LTE model. Electron also decays more slowly in the NCE model than in the LTE model, indicating the possibility of a lower decay rate of the electrical conductivity of CO_2 arc discharge.

2.6. Results of CO_2-PTFE vapor [12]

2.6.1. Byproduct Molecular Species: CO and CF Mole Fraction Variation

Figures 9 and 10 show the time evolution of CO and CF mole fractions, which are key byproducts during arc decay in CO_2 mixed with PTFE vapor. These species are important for understanding recombination dynamics and chemical effects in fluorocarbon-based arc quenching media.

CO forms mainly via CO_2 dissociation followed by C + O → CO recombination. This reaction is exothermic and most active at 4000–8000 K, where

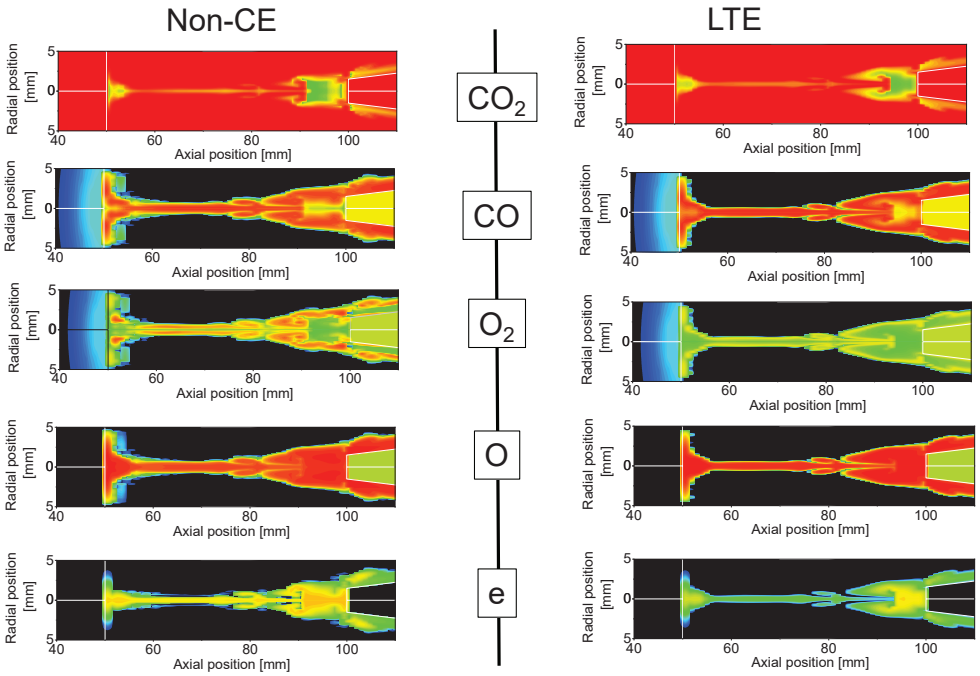

Figure 8. Comparison of calculation results in mole fraction at $t = 100\,\mu s$ in CO_2 arcs by NCE model and LTE model. (100→ 0 A, CO_2 flow velocity 5 m/s) [11].

the plasma is partially dissociated. As the arc cools, CO becomes the dominant carbon species, with increasing mole fraction downstream, particularly near the nozzle throat. CF radicals originate from the decomposition of PTFE ablation products such as C_2F_4, and appear near the arc fringes where temperature and fluorine availability favor their formation. Their mole fraction peaks at t = 50–100 µs, aligning with strong recombination activity. CF then reacts via CF + F → CF_2 or CF + M → CF_2 + M, yielding the more stable CF_2 species.

Crucially, CO and CF contribute to electron density reduction through dissociative attachment: CO + e → C+ O^-, and CF + e → C + F^-. These reactions capture low-energy electrons and form negative ions, particularly as electron temperature drops during arc decay. This leads to rapid electron loss and aids dielectric recovery between electrodes. Modeling such mechanisms is essential for accurately simulating non-equilibrium arc behavior in environmentally friendly C-F-O gas mixtures for circuit breakers.

Monatomic	C, F, O
Diatomic	CF, C_2, FO, F_2, CO, O_2
Triatomic	CF_2, C_2F, C_3, CFO, F_2O, FO_2, CO_2, C_2O, O_3
Tetratomic	CF_3, C_4, CF_2O, C_2F_2, F_2O_2, COF_2, C_2CF, C_2FO
Pentatomic	CF_4, C_2F_3, C_5, C_3O_2, CF_3O
Hexatomic	C_6, C_2F_4, C_3F_3, C_4F_2, CF_3O_2, CF_3OF
Heptatomic	C_7, C_2F_5, C_3F_4
Octatomic	C_8, C_2F_6, C_3F_4O
More than nonatomic	C_9, C_3F_6, C_3F_7, C_4F_6, $C_2F_6O_2$, C_3F_8, CF_3F_5, C_5F_6, C_4F_8, C_6F_6, C_4F_{10}, C_7F_8, C_5F_{12}, C_6F_{14}, C_7F_{16}, C_4F_7O, C_5F_8O, C_5F_9O, C_5F_{10}, $C_5F_{10}O$
Monatomic ion	C^+, C^{2+}, C^-, F^+, F^{2+}, F^-, O^+, O^{2+}, O^-
Diatomic ion	C_2^+, C_2^-, CO^+, O_2^+, O_2^-, O_2^{2-}, CF^+, CF^-
Polyatomic ion	CF_2^+, CF_2^-, CO_2^+, CO_2^-, FCO^-, CF_3^+, CF_3^-, COF_2^+, COF_2^-, $C_3O_2^+$
Electron	e

Table 2. Species considered for composition of CO_2/ O_2/ $C_5F_{10}O$ in the present work [14].

3. Modelling of Arcs in CO_2/ O_2/ $C_5F_{10}O$ with considering irreversible reactions [13, 14]

3.1. Equilibrium composition of CO_2/ $C_5F_{10}O$ or CO_2/ O_2/ $C_5F_{10}O$

To validate the physical assumption of one-way irreversible decomposition of $C_5F_{10}O$ under arc conditions, equilibrium composition calculations were performed for pure $C_5F_{10}O$ as well as its mixtures with CO_2 and O_2 at atmospheric pressure [13, 14]. The molecular constants of $C_5F_{10}O$ and byproducts were newly calculated by quantum chemistry calculations [16] in addition to the data in NIST-JANAF Table [15]. Table 2 shows species considered in the present work.

Figure 11 presents the equilibrium composition of 100% $C_5F_{10}O$ as a function of temperature. At high temperatures exceeding 15,000 K, the plasma consists mainly of monatomic ions (C^+, O^+, F^+) and electrons. As temperature decreases, these ions recombine into neutral atoms (C, O, F), which subsequently asso-

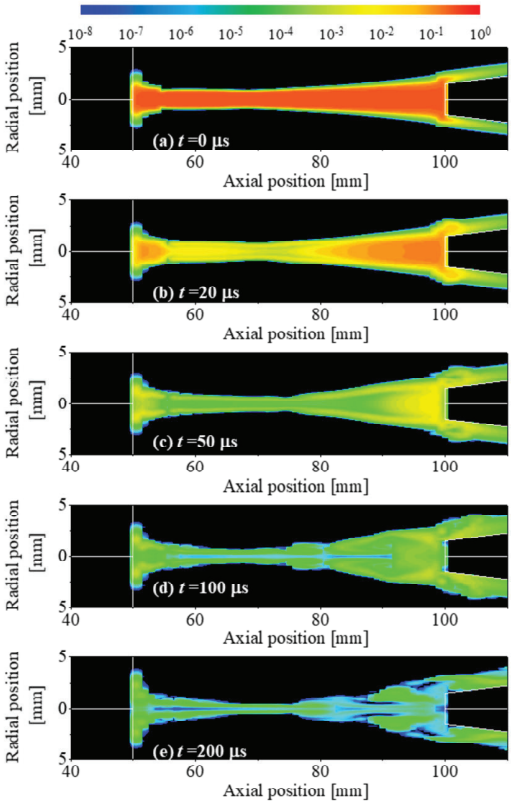

Figure 9. Time variation in distribution of mole fraction of CO under free recovery condition (100→ 0 A, Inlet gas velocity 5 m/s) [12].

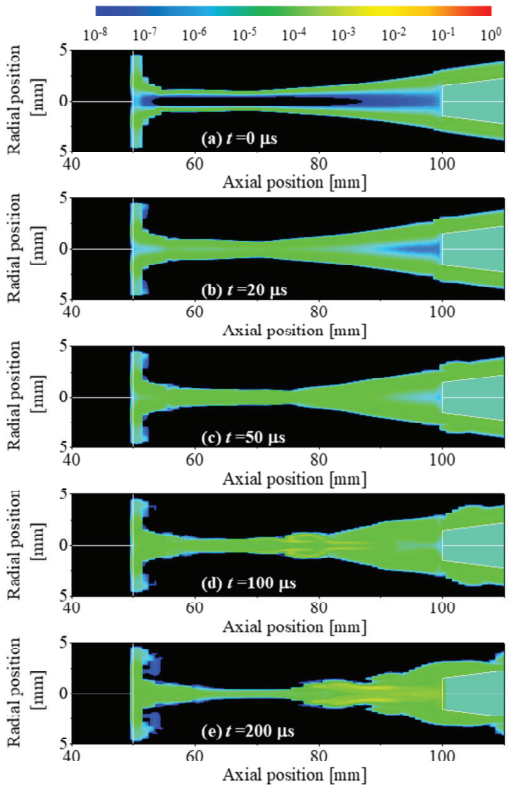

Figure 10. Time variation in distribution of mole fraction of CF under free recovery condition (100→ 0 A, Inlet gas velocity 5 m/s) [12].

ciate to form stable molecular fragments such as CF_4, C_3F_4O, C_5F_8O, and eventually $C_5F_{10}O$ as temperatures approach ambient levels.

However, as shown in Figure 12, the equilibrium composition of a ternary mixture ($75\%CO_2/10\%O_2/15\%C_5F_{10}O$) reveals a contrasting trend. In this case, even after cooling to 300 K, the original $C_5F_{10}O$ species is not re-formed. Instead, fluorinated and oxygenated fragments remain, including COF_2, C_2F_4, C_5F_8O, and other byproducts. This result indicates that, in the presence of CO_2 and O_2, the decomposition of $C_5F_{10}O$ is practically irreversible. Thus, modeling the dissociation as a one-way reaction is physically justifiable.

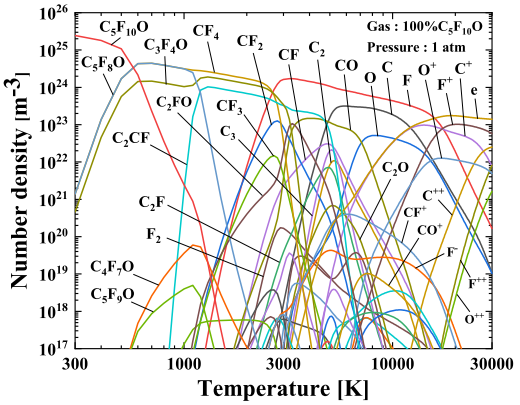

Figure 11. Equilibrium composition of 100%$C_5F_{10}O$ thermal plasma at a pressure of 1 atm [14].

3.2. MODELING OF ARC PLASMA IN A NOZZLE

3.3. Assumptions

Based on the above findings, a simplified thermofluid model incorporating irreversible dissociation is developed. The following assumptions are applied:

(1) The calculation domain has a axisymmetric structure. (2) The arc plasma is under local thermodynamic equilibrium (LTE) condition. (3) The gas flow is laminar, thus the effect of turbulent is neglected. (4) The arc is optically thin. (5) The electrode surface phenomena such as electron emission are not considered. (6) The electric field has only axial direction components. (7) Density fluctuations due to pressure fluctuations in steady state are neglected. (8) Melting or evaporation of the electrodes and nozzle are neglected. (9) Heat conduction inside the electrodes and nozzle is considered. (10) The irreversible reaction such as $C_5F_{10}O$ (A) + CO_2 (B) or CO_2/O_2 (B) → C-F-O byproducts (C: the dissociated gas) is only considered, where A and B are indicators of reactants and C is an indicator of the product in A+B→C reaction, as indicated in Fig. 13.

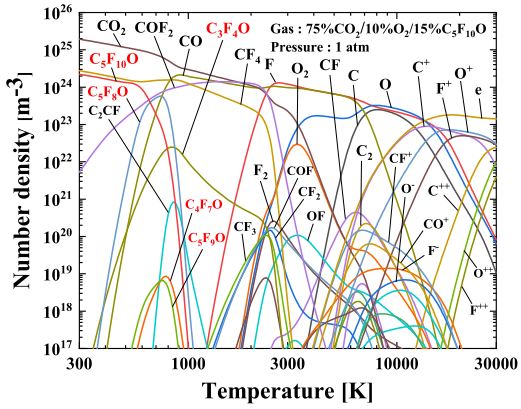

Figure 12. Equilibrium composition of 75%CO_2/ 10%O_2/ 15%$C_5F_{10}O$ thermal plasma at a pressure of 1 atm [14].

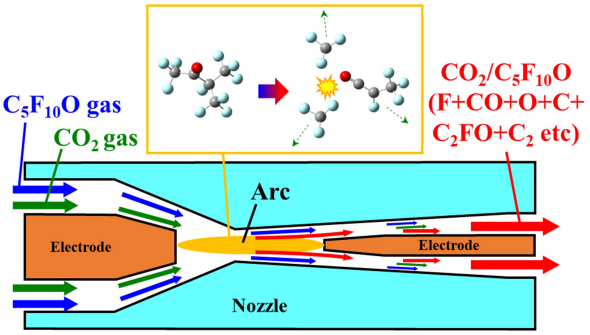

Figure 13. Gas composition calculation considering irreversible dissociation reaction.

3.4. Numerical Modeling and Simulation Conditions

3.4.1. Governing equations

The present model assumes that the arc plasma is governed by the fluid equations such as the mass conservation, the momentum conservation, and energy conservation with electromagnetic fields. In addition to these, the following mass conservation equations were solved:

$$C_5F_{10}O(A) + CO_2/O_2(B) \rightarrow C - F - O \text{ byproducts}(C)$$

$$\frac{\partial(\rho Y_A)}{\partial t} + \nabla \cdot (\rho \boldsymbol{u} Y_A - \rho D_{AB} \nabla Y_A) = -k_A \frac{\rho^2 Y_B Y_A}{m_B} \quad (9)$$

$$\frac{\partial(\rho Y_C)}{\partial t} + \nabla \cdot (\rho \boldsymbol{u} Y_C - \rho D_{CB} \nabla Y_C) = m_C k_A \frac{\rho^2 Y_A Y_B}{m_A m_B} \quad (10)$$

$$Y_B = 1 - (Y_A + Y_C) \quad (11)$$

where Y_X: the mass fraction of gas X, m_X: the mass of particle X [kg], m_{XY}: the relative mass of particle X and Y [kg], D_{XY}: the diffusion coefficient of gas X in gas Y. Thermodynamic and transport properties were calculated for 100%$C_5F_{10}O$ (A), CO_2/O_2 (B) and the dissociated byproducts (C). Solving Eqns.(15) and (16) enables us to consider the irreversible reactions of $C_5F_{10}O$ (A) + CO_2/O_2 (B) $\rightarrow$ the dissociated byproducts (C).

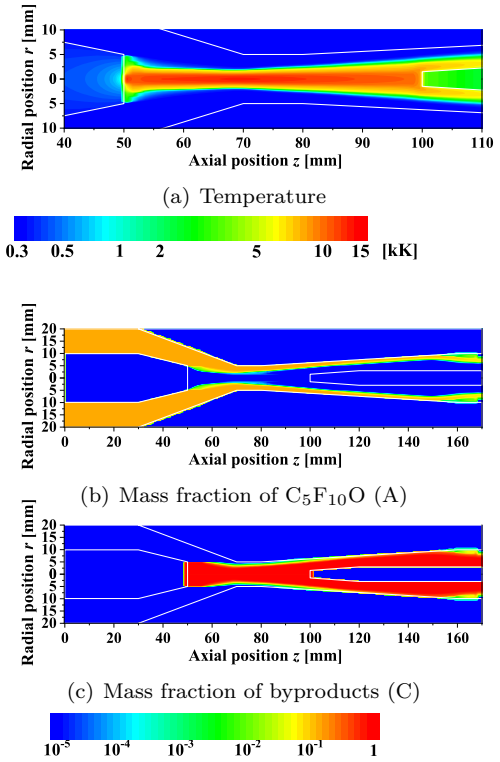

Figure 14. Two-dimensional distributions of arc temperature, mass fraction of $C_5F_{10}O$, and that of byproducts in a steady state in 85%CO_2/15%$C_5F_{10}O$ gas flow [14].

3.4.2. Calculation domain and condition

The geometry and grid used for the simulation is the same to that shown in Figure 3. The computational domain represents a half cross-section of the arc device and includes a 10 mm diameter nozzle throat and 50 mm inter-electrode spacing. Gas enters the domain at $z = 0$ mm with a flow rate of 100 L/min (1.768 m/s) at 300 K. A fixed pressure of 1 atm is applied at the outlet. First, a steady-state arc is simulated with a DC current of 50 A using the SIMPLE algorithm. Then, a transient simulation is initiated at $t = 0$ µs by dropping the current to 0 A to simulate free recovery.

The model captures the arc temperature, flow field, and species concentrations, enabling investigation of the dissociation behavior of $C_5F_{10}O$ and the influence of O_2 addition on arc decay.

3.5. CALCULATION RESULTS

3.5.1. The temperature distributions of CO_2/ $C_5F_{10}O$ or CO_2/ O_2/ $C_5F_{10}O$ in a steady state with consideration irreversible dissociation

Figures 14(a), 14(b), and 14(c) show the steady-state results of the arc in an 85%CO_2 / 15%$C_5F_{10}O$ mixture, including temperature distribution, mass fraction of the reactant ($C_5F_{10}O$, denoted A), and mass fraction of byproducts (denoted C) resulting from irreversible dissociation.

Figure 14(a) indicates a high-temperature arc column concentrated near the nozzle throat at $z \approx 70$ mm, with maximum temperatures reaching 15,000 K. The arc diameter narrows in this region due to strong convection losses induced by high gas velocity.

Figure 14(b) shows that unreacted $C_5F_{10}O$ gas is located primarily on the outer periphery of the arc region, consistent with the thermal dissociation mechanism. In contrast, Figure 14(c) demonstrates that the dissociation products occupy the arc core, where temperatures are sufficient to break C-F and C-O bonds. This spatial segregation validates the modeling assumption that the A+B→C reaction predominantly occurs in the high-temperature zone.

3.5.2. Transient Arc Decay Behavior under Free Recovery Conditions

Figure 15 shows the temporal evolution of the arc temperature distribution from $t = 0$ to 100 µs in the 85%CO_2/15%$C_5F_{10}O$ mixture following current interruption. At $t = 0$ µs, the arc begins from the steady-state condition. Rapid temperature decay is observed near the nozzle throat due to enhanced convective losses in this region.

At $t = 20$ µs, significant cooling has occurred in the high-speed flow region, with localized arc contraction. By $t = 100$ µs, the high-temperature core has largely vanished, and thermal energy is rapidly dissipated into the surrounding gas. This behavior mirrors the cooling dynamics seen in chemically non-equilibrium models, but here the dissociation enthalpy contributes significantly to energy absorption.

3.5.3. Comparison of Arc Decay Rates Across Mixtures

Figure 16 compares the temporal evolution of the axial arc temperature at $z = 70$ mm among three cases of 85%CO_2/15%$C_5F_{10}O$ (with irreversible dissociation), 75%CO_2/10%O_2/15%$C_5F_{10}O$ (with irreversible dissociation), 75%CO_2/10%O_2/15%$C_5F_{10}O$ (without irreversible dissociation, i.e., conventional LTE model).

The addition of O_2 increases the arc decay rate. This is because O_2 dissociation introduces a large specific heat capacity around 4000 K, enhancing energy removal by convection. In the model including irreversible decomposition, the arc cools faster than in the conventional model due to the additional energy consumed by bond-breaking in the $C_5F_{10}O$ molecules.

At $t = 50$ µs, the arc temperature in the O_2-added mixture has already dropped below 8000 K. In contrast, the case without irreversible dissociation retains higher core temperatures. These differences highlight the importance of incorporating both irreversible chemical effects and mixture design in predicting arc extinction behavior.

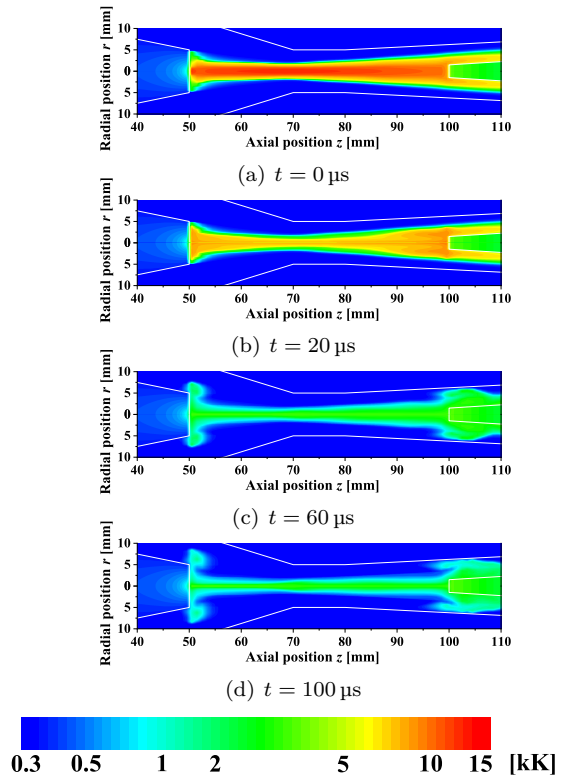

Figure 15. Temporal variation of temperature and flow velocity distribution in 85%CO_2/15%$C_5F_{10}O$ gas arcs [14].

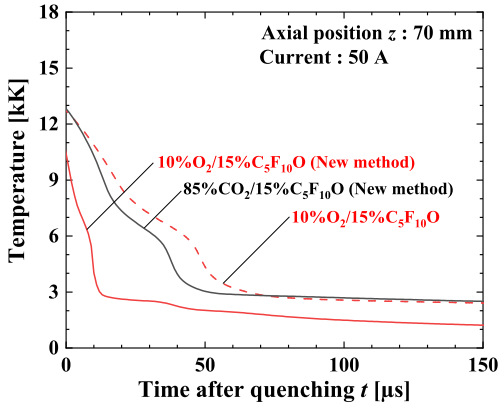

Figure 16. Temperature decrease at the nozzle throat inlet in decaying CO_2/ O_2/ $C_5F_{10}O$ arcs (z = 70 mm) [14].

4. Summary

This study presented two numerical approaches to simulate arc plasma decay phenomena in polyatomic molecular gas flows with a focus on chemically non-equilibrium (CNE) effects and irreversible reactions relevant to SF_6 alternatives.

First, a chemically non-equilibrium arc model was developed for a C-F-O system based on a 90%CO_2

+ 10%C_2F_4 mixture, representing a system where PTFE ablation vapor mixes with CO_2. A set of 24 key species was selected based on equilibrium composition analysis from an original set of 48 candidates. The model incorporated 49 reversible reactions (98 total) with temperature-dependent rate coefficients sourced from established kinetics databases. Using this model, the transient evolution of temperature and species composition during arc decay was simulated under free recovery conditions. The results demonstrated that rapid temperature decay leads to electron–ion recombination and subsequent formation of neutral atoms and stable molecules such as CO, CF, and CF_2. These effects critically influence arc conductivity and chemical byproducts.

Second, a simplified thermofluid model was constructed for $CO_2/O_2/C_5F_{10}O$ mixtures by introducing irreversible dissociation reactions. Thermodynamic equilibrium analysis showed that once $C_5F_{10}O$ is dissociated in the arc core, it does not reform upon cooling, especially in the presence of O_2. This justified modeling the process as a one-way irreversible reaction. The model accounted for the decomposition energy and its contribution to arc cooling. Simulations revealed that the presence of O_2 enhances convective energy removal through its dissociation enthalpy, while $C_5F_{10}O$ decomposition accelerates arc temperature decay through both chemical and thermal mechanisms. Comparative results against conventional LTE models highlighted significant differences in arc temperature dynamics when irreversible chemistry is included.

Overall, the two models provide complementary insights into arc extinction phenomena in alternative gas mixtures for SF_6 replacement. The CNE model captures detailed chemical kinetics under transient non-equilibrium conditions, while the irreversible model offers computational tractability for engineering-scale simulations. These tools are essential for the design and optimization of environmentally friendly switching technologies in high-voltage systems.

References

[1] P. Stoller, M. Dhotre, B. Spreen, and J. Korbel. *SF_6-alternative 145 kV metal-enclosed circuit breaker*. CIGRE 2024 Paris Session, A3-10717-PS2. CIGRE, 2024.

[2] W. Gu, Y. Li, H. Chen, et al. Study on nozzle ablation caused by arcing in high voltage circuit breaker with C4-FN gas mixtures. In *7th Int. Conf. Electric Power Equip. - Switching Technol. (ICEPE-ST 2024)*, pages 415–420, 2024. doi:10.1109/ICEPE-ST61894.2024.10792568.

[3] J. Korbel, J. Ostrowski, P. Stoller, et al. Convective performance of C5-flouroketone-based (C5-FK) and C4-flouronitrile-based (C4-FN) gas mixtures and SF_6. *J. Thermal Sci.& Eng. Appl.*, 15:011001, 2023. doi:10.1115/1.4055330.

[4] R. Girard, J. J. Gonzalez, and A. Gleizes. Modelling of a two-temperature SF_6 arc plasma during extinction. *J.Phys.D:Appl.Phys.*, 32(11):1229–1238, 1999. doi:10.1088/0022-3727/32/11/308.

[5] J. J. Gonzalez, R. Girard, and A. Gleizes. Decay and post-arc phases of a SF_6 arc plasma: a thermal and chemical non-equilibrium model. *J.Phys.D:Appl.Phys.*, 33(21):2759–2768, 2000. doi:10.1088/0022-3727/33/21/314.

[6] Y. Tanaka, Y. Yokomizu, T. Matsubara, and T. Matsumura. Particle composition of two-temperature SF_6 plasma in pressure range from 0.1 to 1 MPa. In *Proc. 12th Int. Conf. on Gas Discharges & Their Appl., Greifswald, Germany*, volume II, pages 566–569, 1997.

[7] Y. Tanaka and T. Iijima. Hybrid thermofluid modeling with LTE and non-LTE assumption for decaying molecular gas arcs. In *The 6th Int. Conf. Electric Equipment -Switching Technol. (ICEPE-ST2022)*, pages 1–0414, 2022. doi:10.1109/ICEPE-ST51904.2022.9757122.

[8] Y. Wu, H. Sun, Y. Tanaka, et al. Influence of the gas flow rate on the nochemical equilibrium N_2 arc behavior in a model nozzle circuit breaker. *J. Phys. D: Appl. Phys.*, 49(42):425202, 2016. doi:10.1088/0022-3727/49/42/425202.

[9] H. Sun, Y. Wu, Y. Tanaka, et al. Investigation on chemically non-equilibrium arc behaviors of different gas media during arc decay phase in a model circuit breaker. *J. Phys. D: Appl. Phys.*, 52(7):075202, 2019. doi:10.1088/1361-6463/aaf51f.

[10] H. Sun, Y. Zhang, Y. Wu, et al. Numerical modeling of CO_2 arc based on the non-chemically equilibrium effect. *J. Phys. D: Appl. Phys.*, 55:225201, 2022. doi:10.1088/1361-6463/ac55c0.

[11] Y. Tanaka. Development of chemically non-equilibrium modeling for decaying CO_2 arcs with reaction rates. In *Int.Workshop on High Voltage Eng. (IWHV2022)*, volume EPP-22-103, SP-22-038, HV-22-084, pages 61–66, 2022.

[12] Y. Tanaka and T. Iijima. Advancements in modeling chemically non-equilibrium decaying arc plasmas in C-F-O gas mixtures. In *2024 7th International Conference on Electric Power Equipment - Switching Technology (ICEPE-ST)*, pages 397–402, 2024. doi:10.1109/ICEPE-ST61894.2024.10792462.

[13] H. Kai, Y. Nakano, Y. Tanaka, and T. Ishijima. Advancements in modeling chemically non-equilibrium decaying arc plasmas in C-F-O gas mixtures. In *Int.Workshop on High Voltage Eng. (IWHV2022)*, volume EPP-22-104, SP-22-039, HV-22-085, 2022.

[14] H. Kai, F. Demura, Y. Nakano, et al. Numerical calculation of decaying gas-blast arcs in CO_2/ O_2/ $C_5F_{10}O$ with different gas mixture ratios. In *The 23rd Int. Conf. Gas Discharges & Their Applications (GD2023), Greifswald, Germany*, pages 140–143, 2023.

[15] M. W. Chase. NIST-JANAF Thermochemical Tables. In *J Phys. & Chem. Ref. Data*, Monograph, No. 9. National Inst. of Standards & Technol., 1998.

[16] Gaussian 16, Revision B.01. Frisch, M. J. et all. Gaussian, Inc., Wallingford CT (2016). arXiv:https://gaussian.com/gaussian16.